Author Manuscript

Author Manuscript

Author Manuscript

Author Manuscript

HHS Public Access

Author manuscript

Biomaterials. Author manuscript; available in PMC 2019 April 01.

Published in final edited form as:

Biomaterials. 2018 April ; 161: 117–128. doi:10.1016/j.biomaterials.2018.01.025.

Unique electrophysiological and impedance signatures between encapsulation types: An analysis of biological Utah array failure and benefit of a biomimetic coating in a rat model

Patrick A. Cody[a,c], **James R. Eles**[a,c], **Carl F. Lagenaur**[b], **Takashi D. Y. Kozai**[a,c,d,e], and **X. Tracy. Cui**[a,c,d,*]

[a]Department of Bioengineering, University of Pittsburgh, 5057 Biomedical Science Tower 3, 3501 Fifth Avenue, Pittsburgh, PA 15260, USA

[b]Department of Neurobiology, University of Pittsburgh, Pittsburgh, PA, USA

[c]Center for the Neural Basis of Cognition, University of Pittsburgh, Pittsburgh, PA, USA

[d]McGowan Institute of Regenerative Medicine, University of Pittsburgh, Pittsburgh, PA, USA

[e]NeuroTech Center, University of Pittsburgh Brain Institute, Pittsburgh, PA, USA

Abstract

Intracortical microelectrode arrays, especially the Utah array, remain the most common choice for obtaining high dimensional recordings of spiking neural activity for brain computer interface and basic neuroscience research. Despite the widespread use and established design, mechanical, material and biological challenges persist that contribute to a steady decline in recording performance (as evidenced by both diminished signal amplitude and recorded cell population over time) or outright array failure. Device implantation injury causes acute cell death and activation of inflammatory microglia and astrocytes that leads to a chronic neurodegeneration and inflammatory glial aggregation around the electrode shanks and often times fibrous tissue growth above the pia along the bed of the array within the meninges. This multifaceted deleterious cascade can result in substantial variability in performance even under the same experimental conditions. We track both impedance signatures and electrophysiological performance of 4×4 floating microelectrode Utah arrays implanted in the primary monocular visual cortex (V1m) of Long-Evans rats over a 12-week period. We employ a repeatable visual stimulation method to compare signal-to-noise ratio as well as single- and multi-unit yield from weekly recordings. To explain signal variability with biological response, we compare arrays categorized as either Type I, partial fibrous encapsulation, or Type II, complete fibrous encapsulation and demonstrate performance and impedance signatures unique to encapsulation type. We additionally assess benefits of a biomolecule coating intended to minimize distance to recordable units and observe a temporary improvement on multi-unit recording yield and single unit amplitude.

*Corresponding Author. 5057 Biomedical Science Tower 3, 3501 Fifth Avenue, Pittsburgh, PA, USA. xic11@pitt.edu; Fax: +1-412-648-9076; Tel: +1-412-383-6672.

Publisher's Disclaimer: This is a PDF file of an unedited manuscript that has been accepted for publication. As a service to our customers we are providing this early version of the manuscript. The manuscript will undergo copyediting, typesetting, and review of the resulting proof before it is published in its final citable form. Please note that during the production process errors may be discovered which could affect the content, and all legal disclaimers that apply to the journal pertain.

Author Manuscript Author Manuscript Author Manuscript Author Manuscript

1. INTRODUCTION

Intracortical microelectrode arrays (MEA) remain the most common choice for obtaining high dimensional recordings of spiking neural activity with nonpareil spatiotemporal resolution [1, 2]. MEA recording fidelity is vital for their long-term clinical use in brain computer interface (BCI) based prosthetics as well as in basic research for understanding the neural ensembles that generate behavior [3]. The Utah MEA, a prevalent option for both clinical and non-human primate research, consists of a 'floating' 10 × 10 bed of needles design (tethered via wire-bundle to a pedestal anchored to the skull) and remains unchanged for over 15 years (since the switch to parylene-C electrode insulation in 2002) save for minimal modifications in fabrication and wire insulation. Despite widespread use and established design; mechanical, material and biological challenges persist that contribute to a steady decline in performance [diminished signal amplitude and recorded cell population] or outright array failure [4, 5]. In a clinical context the array must be functional throughout the patient's lifetime. Mechanical challenges such as acute physical insults to wiring, tethering and the implant itself can be unavoidable and inherent to experimental preparation and surgery. Material failures are attributed to foreseeably tractable design limitations [6]. Chronic biological failures/challenges beyond acute infection or bleeding persist in this design context regardless of optimal material design [7]. Chronic biological failures typically occur in two locations: at the neural tissue surrounding the electrode sites and/or within the meninges at the platform of the implant. Implantation/insertion injury is associated with acute neuronal cell death, mechanical inflammatory activation, as well as blood-brain-barrier and vascular damage in the vicinity of the electrode shank [8]. Resultant bleeding, protein adsorption, inflammatory cell influx and continued mechanical mismatch contribute to a persisting inflammatory environment characterized by activated microglia and astrocytes that ensheath the electrodes and putatively contribute to degeneration and increased distance to neural recording targets surrounding the electrode [9–11]. This multifaceted deleterious cascade can result in substantial variability in performance even under the same experimental conditions [8, 12]. Biological insult above the pia compounds variability further as arrays become encapsulated to a varying extent by fibrous tissue (consisting mostly of type-1 collagen) and a portion of arrays are liable to gross array movement and eventual ejection owing to a combination of complete fibrous encapsulation and dura regrowth [4, 13–17].

Novel subcellular electrode designs, such as carbon fiber arrays, drastically reduce blood-brain-barrier disruption and mechanical mismatch thereby limiting much of the inflammatory impact at the electrode site and along the shank [18]. Nonetheless, the tissue environment surrounding these probes still presents glial activation (increased activated astrocyte expression in the case of carbon fiber electrodes) and the implant portion spanning the pia to dura is still subject to dura regrowth and fibrous accumulation. Fibrous tissue growth is evident even in devices designed to minimize recording substrate footprint (such as mesh micro-electrocorticography arrays [micro-ECoG]) [19]. Furthermore, long-term stability of these devices remains to be evaluated [7, 18, 20]. An optimal solution to the aforementioned biological challenges would involve a facile surface modification method that is amenable to current commercial arrays and combats both biological failure points to

Author Manuscript Author Manuscript Author Manuscript Author Manuscript

minimize electrode site-to-neuron distance and fibrotic encapsulation to maximize recording performance. Approaches for commercial implants have mainly been focused on surface modifications at electrode sites using conductive polymers, anti-inflammatory compounds and bioactive compounds [21–26]. Extracellular matrix proteins such as laminin have been thoroughly explored owing to their supporting role as a neural growth substrate [24, 27–29]. Laminin has been demonstrated to significantly reduce microglial and astrocytes activation both at 1 day and 4 weeks post implant, but has no benefit on neuron density or proximity [27]. Neural cell adhesion molecules similarly promote neurite outgrowth. In vitro, L1 cell adhesion molecule (L1CAM) coated surfaces, yield less astrocyte attachment and increased neurite length compared to laminin [26]. In vivo, L1CAM coated surfaces result in reduced gliosis and increased neural density at electrode sites up to 8 weeks after implantation. Additionally, two-photon imaging reveals that L1CAM coated implants present significantly less microglial process attachment and spreading during acute implantation. In this study we intend to evaluate in vivo recording benefits of L1CAM coated 4×4 Utah style arrays over a chronic period in rats using a visually evoked recording paradigm.

We find that L1CAM does result in an acute recording benefit. However the effect is quickly overwhelmed by a high prevalence of substantial array encapsulation and ejection. We show that electrophysiology performance is unique to the degree of encapsulation determined at endpoint and that this in conjunction with impedance features may be used to inform the tissue environment and implant outcome without additional endpoints.

2. METHODS

A total of nine Long-evans rats were implanted with either L1CAM coated or uncoated (see Table 1 and Supplementary Table 1) 4×4 Blackrock arrays from which impedance and electrophysiology data were recorded weekly for 12 weeks beginning on week 0, one day after surgery. Ex-vivo micro computed tomography (micro-CT) imaging was performed on arrays in an intact head preparation at 4 weeks and 12 weeks. Second-harmonic generation (SHG) imaging was used for qualitative characterization of the encapsulation features of representative arrays within headcaps. All animal care and procedures were performed under the approval of the University of Pittsburgh Institutional Animal Care and Use Committee and in accordance with regulations specified by the Division of Laboratory Animal Resources.

2.1 ARRAYS AND COATING

4×4 Utah arrays were purchased from Blackrock Microsystems, Salt Lake City, UT. These arrays consist of 16 parylene-C insulated 1.0 mm long platinum electrodes spaced 400 μm apart and organized into a 4×4 square bed-of-needles design. Arrays were ETO sterilized then either implanted as is, or coated with L1CAM protein. L1CAM solution was prepared as described previously [26, 30, 31]. Briefly, rat pup brain tissue homogenate was passed over an affinity column of L1CAM antibody and L1CAM was then eluted into a buffered solution. The coating procedure is described as follows: under sterile conditions, arrays were exposed to 1 minute of oxygen plasma in a radio frequency glow discharge plasma chamber

Author Manuscript Author Manuscript Author Manuscript Author Manuscript

and then dipped into the L1CAM solution for 30 minutes at room temperature followed by a sterile phosphate buffered saline (PBS, pH7.4) wash and implantation.

2.2 SURGERY

Five uncoated arrays and four L1CAM coated arrays were implanted into the primary monocular visual cortex (V1m) of adult Long-Evans rats (1 array per animal; see results section 3.2 for explanation of sample number). Rats were induced at 2.5% isoflurane then maintained at 1.5% isoflurane for anesthesia. Body temperature was maintained using a warm water pad (Jorvet HTP-1500, Jorgensen Labs, Loveland, CO) throughout the surgery. After mounting the rat onto a stereotaxic frame the skull was exposed and a [~6 mm × 5 mm] craniotomy was prepared at 5.5–8.5 posterior and 2–4.5 lateral to bregma using a high-speed dental drill with a 0.7mm size drill bit. The craniotomy was intermittently cooled using sterile saline to minimize heat damage from the drill. A burr drill was then used to prepare 4 bone screw holes for securing the headcap: 2 anterior bilaterally over the motor cortex, 1 posterior and ipsilateral to the craniotomy, and another over the contralateral visual cortex. The duraotomy was prepared with angled microscissors after an initial incision with a 30G needle. Once exposed, the tissue was kept moist and covered with sterile saline saturated gel-foam. The array was oriented using a vacuum syringe mounted on a stereotaxic arm and situated such that the side opposite the array wire bundle was parallel with the anterior edge of the craniotomy with electrode tips barely resting on the cortical surface as viewed under a surgical scope. The array was then inserted into the cortex by turning the stereotaxic ventral adjustment to a depth of 1 mm at a rate of 1 mm/min (as per vendor recommendation for rodent applications) and the wire bundle was secured with UV cured dental cement. After applying a small dab of Kwik-Sil (World Precision Instruments; Sarasota, FL) to the front edge of the array the vacuum syringe for placement was removed and the entire craniotomy was covered over with Kwik-Sil. Stainless steel skull screws were then inserted and the connector was oriented orthogonal to midline just behind the anterior bilateral bone screws. The ground wire was connected to the anterior screw ipsilateral to the implant while the reference wire was connected to the posterior screw contralateral to the implant. The headcap was prepared with multiple layers of dental cement to secure the screws and craniotomy. Skin was secured around the headcap using a basket suture. Triple antibiotic ointment was applied around the wound and 5 mg/kg ketofen was injected intraperitoneally (IP) upon finishing surgery and then for three consecutive days after surgery.

2.3 IMPEDANCE SPECTROSCOPY

For each weekly recording session, animals were induced at 2.5% isoflurane anesthesia then maintained at 1.5% isoflurane to perform electrochemical impedance measurements before electrophysiology recordings. Arrays were connected to an Autolab potentiostat via a 16-channel multiplexer and impedance was measured sequentially for each channel using a 15 multi-sine wave paradigm at 10 mV RMS amplitude spanning frequencies from 10 Hz to 32 kHz.

Author Manuscript Author Manuscript Author Manuscript Author Manuscript

2.4 ELECTROPHYSIOLOGY RECORDING

Electrophysiology data were collected as described in [32]. Briefly, following impedance measurements, isoflurane was reduced to ~0.8–1.2% in an effort to minimize phasic firing and maximize spontaneous activity while providing sufficient anesthesia to maintain the rats in an inactive state. Electrophysiology data were recorded first during spontaneous conditions (data not shown) in a dark room and then while evoking activity with delay corrected transistor-transistor logic (TTL) trigger time-stamped visual stimuli presented with an LCD monitor to the eye contralateral to the implant. All presented electrophysiology data were recorded during the evoked session. Stimuli consisted of 8 repeats of a randomly ordered sequence of 8 directions (360°/45° = 8 directions) of moving square-wave gratings lasting 1 second (‘ON’ state; 3 cycles per second, 2.5 cm wide bars at 100% contrast) followed by 1 second of a blank black screen (‘OFF’ state). The voltage stream was filtered for LFP (1–100 Hz) and spike data (300–5000 Hz). Spike sorting was initially automated offline using principal-component-analysis (PCA) and k-means clustering with a custom MATLAB script followed by manual verification of single-units to obtain final electrophysiology metrics.

Neural signals were acquired through an active Medusa preamplifier, passed through an anti-aliasing filter and digitized at 24,414 Hz then sent to a RX7 recording system (Tucker-Davis Technologies, Alachua, FL). Single-units were initially identified as having crossed a threshold set at 3.5 standard deviations below the mean of the spike data and were centered in a 1.2 msec waveform snippet that was then removed from the spike voltage stream data to calculate mean peak-to-peak noise. PCA was used to reduce isolated waveform dimensions into 3 principal components which were then sorted into separable clusters using k-means clustering. Single-units were verified manually with 3D PCA plots, autocorrelograms, and peri-stimulus-time histograms in addition to mean and pile waveform plots. All reported electrophysiology metrics were calculated as defined in [32], but calculations will be briefly outlined here again for convenience. Single unit signal-to-noise amplitude ratio (SU SNAR) was calculated from verified units as peak-to-peak amplitude of the mean waveform of the isolated cluster divided by two times the standard deviation of the voltage data after removing 1.2 msec threshold crossing waveforms. A channel without a confirmed single-unit is considered to have an SNAR and amplitude of 0 and 0 V respectively. A channel is considered to have evoked multi-unit (MU) activity if MU spike count (from total threshold crossings) is significantly different ($p<0.05$) in a 550 msec bin 50 msec after stimulus onset (during ‘ON’ state) from MU spike count in a 550 msec bin 50 msec before stimulus onset (during ‘OFF’ state) as determined using a paired t-test. MU signal-to-noise firing rate ratio (MU SNFRR) is defined as the average firing rate during the ‘OFF’ state subtracted from the average firing rate during the ‘ON’ state then divided by the average standard deviation of both the ‘ON’ and ‘OFF’ state. Noise amplitude is calculated as mean peak-to-peak amplitude of the spike filtered voltage signal following removal of threshold crossing 1.2 msec waveform snippets.

2.5 HISTOLOGY

Following week 12 electrophysiology and impedance recordings, rats were deeply anesthetized with an IP injection of 50 mg/kg ketamine and 5 mg/kg xylazine in sterile

Author Manuscript Author Manuscript Author Manuscript Author Manuscript

saline. Rats were then perfused with phosphate buffered saline (PBS) followed by 4% paraformaldehyde (PFA). The head was removed and placed in 4% PFA for 2–4 hrs for post-fixation. Prior to dissection, one animal was imaged with micro-CT. One additional rat was implanted with an uncoated array and sacrificed at 4 weeks exclusively for micro-CT scanning. Heads were dissected from the ventral side to preserve the dorsal brain tissue/headcap interface. Brains were finally carefully separated from headcaps and allowed to incubate overnight in 15% sucrose in PBS followed by a 48 hr incubation in 30% sucrose in PBS until embedment and freezing in optical cutting temperature compound (OCT; Fisher Healthcare Tissue Plus) media. Headcaps were scored for encapsulation type, stored in PBS, imaged with second-harmonic generation (SHG) microscopy, and then preserved in PBS with 0.01% sodium azide.

2.6 IMAGING

2.6.1 Second-harmonic generation imaging—Second harmonic generation (SHG) imaging was performed with a two-photon laser scanning microscope comprised of a Ti:sapphire laser (Mai Tai DS; Spectra-Physics, Menlo Park, CA) tuned at a wavelength of 900 nm, a scan head (Prairie Technologies, Madison, WI), two non-descanned photomultiplier tubes (Hamamatsu Photonics KK, Hamamatsu, Shizuoka, Japan) in whole-field detection mode for light collection, and Prairie View software. Z-stack images covered an area of 1157 × 1157 um (512 × 512 pixels).

2.6.2 Micro computed tomography—Micro computed tomography (microCT) was performed with a multi-modal Siemens Inveon micro-CT/SPECT/PET system (Inveon, Siemens Inc., Knoxville, TN, USA) to image implants within an intact head preparation following perfusion with PBS and 4% PFA, but before explantation for histology. The following parameters were used: 360 projection, 2×2 binning, 31 μm pixel size/isotropic resolution, 45.23 mm transaxial field of view (FOV), 2880 transaxial pixels, 32.16 mm axial FOV, 2048 axial pixels, 80 KV voltage, 500 μA current, and 560 ms exposure time.

2.7 STATISTICS

Lumped (group-wise) comparisons between treatments over time were compared using an unbalanced two-way ANOVA. Post-hoc multiple comparisons were done using Bonferroni corrected two-tailed t-tests for repeated hypothesis testing. Where noted, Student's two-tailed t-tests were performed for treatment comparisons at individual weeks. For ANOVA and individual t-tests α=0.05, Bonferroni corrected calculated α=0.0038 based upon α=0.05.

3. RESULTS

3.1 OVERVIEW

To evaluate potential long-term recording benefits of L1CAM, we implanted L1CAM coated and uncoated 16-channel 4×4 bed of needles style arrays from Blackrock Microsystems into the primary monocular visual cortex of Long-Evans rats. These devices were chosen for their comparable design to 96-channel Utah arrays, which are widely used in both non-human primate and clinical research. Despite statistically significant improvement in

Author Manuscript Author Manuscript Author Manuscript Author Manuscript

electrophysiological metrics from L1CAM coated arrays compared to uncoated arrays, recording performance for both groups declined throughout the 12-week study. At endpoint, all implants from both groups were, to a varying extent, enmeshed within the meninges in a tissue-layer consisting largely of collagen positive tissue (Figure 1, bottom SHG images). By gross visual inspection, we determined that this tissue either partially (Type 1 encapsulation) or fully (Type 2 encapsulation) separated the implants from the brain (Figure 1). In the case of Type 1 encapsulation, one or more electrode sites protrude beyond the encapsulation tissue on the ventral surface of the headcap (Figure 1: left). In contrast, Type 2 encapsulated implants had all 16 electrode sites fully encapsulated within the fibrous tissue and are not visible from the ventral surface of the headcap at (Figure 1: right). Type I implants result in defined electrode tracts in transverse histology slices, while type II implants yield a broad circular absence of tissue encompassing the entire implant size (Supplementary Figure 1).

These results suggest that failure of electrophysiological performance in L1CAM coated and uncoated devices was potentially caused by device ejection from the brain owing to ingrowth of encapsulation tissue. To confirm that devices were ejected from the brain, we conducted microCT imaging of an intact animal head at 12 weeks post-implant (Figure 2: bottom). Imaging revealed that the implant was fully ejected from brain tissue and upon dissection it was confirmed that this array presented Type 2 encapsulation. MicroCT imaging of an animal at 4-weeks post-implant revealed that gross array displacement from the initial implant depth was evident by one month (electrophysiology and impedance data from this implant were not included in analyses; Figure 2: top).

3.2 ELECTROPHYSIOLOGY

Electrophysiology recording performance was evaluated from all implants during a visual stimulation paradigm of drifting square-wave gratings for 12 weeks beginning at week 0 (1 day following surgery). For L1CAM coating comparisons, uncoated n=5 and coated n=4. An additional uncoated array was implanted because one uncoated array presented excessively high magnitude (z-score > 2.5) impedance and discontinuous Nyquist plots beginning at week 4. Electrophysiology data from this animal was kept in electrophysiology analyses because is unlikely that noise, light, or movement artifacts present in the spike bandwidth would be coordinated in such a time and stimulus dependent manner to approximate evoked neural activity and spuriously yield significant threshold crossing differences necessary to contribute to MU yield. For encapsulation comparisons, Type 1 n=5 and Type 2 n=4 (see Table 1 for type counts respective to coating treatment).

3.2.1 L1CAM coating improves electrophysiology performance at acute time points—

Spike data analysis of visually evoked activity in V1m revealed a group-wise significant effect of coating treatment on MU yield ($p=0.0114$) and SU SNAR ($p<0.0001$), while no significant differences were observed for SU yield (Figure 3). Performance across all metrics significantly declined from implant to endpoint (MU and SU yield: $p=0.0002$; SU SNAR: $p<0.0001$). MU yield declined sharply from week 4 to week 6, SU yield and SU SNAR declined sharply from week 0 to week 3 then again from week 4 to week 6. Bonferroni corrected pairwise multiple comparison tests (using two-tailed t-tests) indicated significantly greater SU SNAR ($p<0.001$) from coated implants during the first week of

Author Manuscript Author Manuscript Author Manuscript Author Manuscript

recording (Figure 3c; week 0; see representative units in Supplementary figure 2), while no corrected pairwise significance was evident for MU yield between treatments at individual weeks (Figure 3a).

3.2.2 Recording performance differs between encapsulation types—To assess the effect of encapsulation type on recording performance, we compared electrophysiological performance metrics between animals with Type 1 and Type 2 encapsulation. A trend for a divergence in performance between types was evident as early as week 5 for SU metrics (Figure 4c–d) and began at week 6 for MU metrics (Figure 4a–b); Type 2 implants exhibited a sharp decline in performance, while Type 1 implants diminished in performance at a slower rate. Type 2 implants failed to record single-units from week 6 onwards while Type 1 implants continued recording single-units up to endpoint (Figure 4 c–d).

There is an overall significant effect of encapsulation type across all weeks on MU yield, MU SNFRR, SU yield, and SU SNAR ($p=0.0038$, $p=0.0001$, $p=0.0099$, and $p=0.0472$ respectively; Figure 4). Despite significant group-wise effects of SU and MU yield, performance between types is similar up to week 4 (Figure 4 a,c; see also Supplementary table 1 and representative units in Supplementary figure 2). Bonferroni corrected pairwise multiple comparison tests (using two-tailed t-tests) did not reveal any significant differences between types for individual weeks.

3.3 IMPEDANCE

Impedance was recorded weekly at frequencies from 10 Hz to 32 kHz before electrophysiology recordings to monitor electrochemical changes at the implant for comparison to physical implant differences. For L1CAM coating comparisons, the uncoated group had n=5 during weeks 0–3 and n=4 from week 4 onwards, while the L1CAM coated group had n=4 for all weeks. Data from one of the uncoated array animals exhibiting a Type 2 encapsulation type was excluded beginning on week 4 through to all of the remaining weeks due to excessively high magnitude (z-score > 2.5) and noisy/discontinuous impedance recordings. This animal was not excluded from electrophysiology analyses because MU activity was still present until endpoint. For encapsulation type comparisons, the Type 1 group had n=5 for all weeks and the Type 2 group had n=4 for weeks 0–3 and n=3 for week 4 onwards. Recordings (from a single channel on a given week) with magnitude impedance greater than 2.5 MΩ at 1 kHz were removed from all analyses.

Lumped impedance magnitude at 1 kHz from both groups (Figure 5a) exhibits a sharp increase from week 0 to week 1 followed by a downward trend with a salient drop between weeks 3 and 4. The magnitude impedance drop precedes the MU yield drop by 1 week. While there was an absence of overall significant group-wise coating effects on magnitude impedance at 1 kHz, there is a trend for increased impedance magnitude on coated implants for week 0 and 1 that could be attributable to the resistive protein coating [33]. This difference diminished quickly to be insignificant following week 1. On the contrary, there was a significant group-wise effect of encapsulation type on impedance magnitude at 1 kHz (Figure 5c; $p < 0.001$). Bonferroni corrected pairwise multiple comparison tests (using two-

Author Manuscript Author Manuscript Author Manuscript Author Manuscript

tailed t-tests) indicated significantly greater magnitude impedance from Type 1 implants on several individual weeks (0, 4–8, and 10–12; all at $p < 0.002$) following week 1 before which the magnitude impedance between types was indistinguishable. The divergence in impedance magnitude between types began at week 2 (Figure 5b), about 3–4 weeks before electrophysiology performance began to diverge (Figure 4).

Impedance spectra (Nyquist, Bode and phase plots) were analyzed for all channels at each week and compared between encapsulation types (Figure 6a–b). Impedance measurements with discontinuous Nyquist plots akin to traces from channels with a faulty connection or mechanical channel failure were removed from impedance analyses. One channel from an array of each encapsulation type was selected that is representative of overall Nyquist trends unique to encapsulation type. The pronounced semicircular feature at mid to high frequencies of the Type 1 Nyquist traces is a consistent salient distinguishing feature between types (Figure 6a). For the representative channel shown (same location and channel on both arrays), the semicircular diameter is greatest at earlier time points (weeks 1 and 2). The upward (increasing $-Z''$) and rightward (increasing Z') shift (herein referred to as 'northeast') in impedance at 1 kHz (shift upward and toward the imaginary axis [$-Z''$]) scales with the diameter of the semicircle, such that a trace with a more pronounced semicircle (Figure 6a; week 1 – red), will exhibit a greater northeast shift in impedance at 1 kHz (black dot). While a semicircular feature is still present in Type 2 traces, the diameter is much smaller, evident only within a higher frequency region, and 1 kHz impedance values remain in a smaller cluster (Figure 6b).

If Nyquist traces from all channels are averaged between types at each week (Figure 7: left), this discriminating semicircular feature is apparent for all animals as early as week 2 and persists until endpoint, while most apparent at week 8. The semicircular feature is less apparent than in the representative traces (Figure 6ab) owing to variation between implants, but the northeast shift in impedance at 1 kHz (Figure 7: left; green dot) is consistent with this feature (as described for figure 6).

Type 1 impedance Nyquist traces tended more toward the real (resistive) axis (Figure 7: left) and phase plots are less phase shifted (Figure 7: middle) at lower frequencies beginning at week 0 and persisting until endpoint. The range of frequencies over which Type 1 phase plots exhibited lesser phase shifts becomes broader at later time points (Figure 7&8: middle).

While magnitude impedance differences at 1 kHz between types were not evident at week 0 (Figure 5b), it is evident in the Bode plot of week 0 (Figure 7: top right) that Type 2 implants tend towards higher magnitude impedance values at frequencies below 100 Hz. This is evident only at week 0, after which Type 1 magnitude impedance tends to be higher across the majority of the recorded frequency range (Figure 7: bottom right).

Author Manuscript Author Manuscript Author Manuscript Author Manuscript

4. DISCUSSION

4.1 L1CAM improves acute electrophysiology recording

While previous work has histologically demonstrated L1CAM benefits in reducing glia and maintaining greater neuronal density near probe implant site from acute through a chronic period [25, 31], this study is the first to evaluate the impact of an L1CAM coating on electrophysiology recording performance. Our results show improved recording performance from L1CAM coated arrays on the first day of recording as evidenced by increased MU yield and SU SNAR (Figure 3). Improvement at this time point occurred regardless of encapsulation type. This is likely because there is no significant development of encapsulation tissue in the first days post-implant [34]. A prominent feature of L1CAM coated probes in the acute period post-implant is a significant reduction in probe surface area coverage by microglia processes and a significant reduction of microglia signal within up to 20 μm of the probe [35]. The initial increased SU SNAR and MU yield could be explained by this acute reduction of microglial process infiltration at and near recording sites. Microglial process infiltration may both contribute to an increased barrier between healthy neurons from the recording sites thereby influencing recording performance. Further, inflammatory cytokine and reactive oxygen species release from activated microglia/macrophage may influence neural activity [36].

SU yield was not affected by the coating, which may be due to the large observed variability in SU yield. Large SU metric variability is to be expected over the acute recording period [12, 32], enough to obscure yield, but not SU SNAR [12]. Using the same stimulation paradigm in mice, we have demonstrated depth dependence of SU yield within the V1m region, while MU activity was relatively consistent across cortical layers [12, 32]. Subtle differences in implantation depth from insertion variability or variability in bleeding related array expulsion pressure [8] could therefore have contributed to SU yield variability despite fixed and consistent electrode length.

The 4×4 planar bed-of-needles electrode design by Blackrock was chosen to model the most commonly used 10×10 Utah array in clinical BCI studies as closely as possible while adhering to the smaller rat model form factor to enable higher throughput analyses. Similarly, for clinical relevance, a tractable dipcoating approach following oxygen plasma treatment was chosen for safe and facile probe modification upon the day of implantation surgery. The oxygen plasma treatment method to modify parylene-C surfaces with proteins, L1CAM in this case, has been shown to yield covalent linking, however such linkages are in combination with non-covalent adsorption [37, 38]. Previous work has confirmed that the surface bound L1CAM remains attached and bioactive after 5 days of soaking in media at 37 °C. It is perceivable that in the hostile *in vivo* environment, protein coating may degrade more rapidly due to desorption and degradation by reactive oxygen species and proteases. Despite this, the benefit of the L1CAM coating on parylene-C insulated microwire electrodes was demonstrated at 4 weeks following implantation [31]. It is possible that modulating the early tissue response led to a longer lasting benefit. The short duration of recording benefits may be attributable to two factors, degradation of the protein coating and gross array ejection. To improve the coating stability, methods need to be developed to

Author Manuscript Author Manuscript Author Manuscript Author Manuscript

increase the protein binding stability and protein stability or identify stable small molecules that mimic the function of the protein. Gross array movement and eventual ejection (Figure 2) is the second factor that precludes an objective chronic comparison between coating treatments. While we observed overall improved SU recording performance compared to previous reports [14], as demonstrated by greater SU yield overall and consistent SU yield to 12 weeks (from Type 1 arrays), a significant drop in performance was nonetheless observed between weeks 4–6 by which point we observed array displacement from the original implantation depth (Figure 2: top; array bed receded out of skull) and eventual ejection into the headcap by week 12 (Figure 2: bottom). Further studies are needed that address these factors to better evaluate coating influence on electrophysiology recordings and finally coating impact on BCI task performance.

4.2 Encapsulation outcome and recording variability

Array categorization into encapsulation types enables a disentanglement of electrophysiology performance variability, as evident from significantly different electrophysiological performance outcomes in both MU and SU metrics between arrays categorized as Type 1 versus those categorized as Type 2 (Figure 4). While significant pairwise differences are absent, a trend for a divergence of recording performance is evident in all metrics beginning at week 6 (Figure 4). The comparable SU and MU yield between types up to week 4 (Figure 4 a,c and Supplementary Table 1) could suggest that all arrays upon implantation were type 1 until developing into type 2 in the following weeks. However, it could also be the case that implantation differences beyond the control of surgical practice (e.g. vasculature differences) resulted in tissue differences respective to type upon implantation that are not reflected in recording metrics or do not acutely influence recording performance [8]. If the former were to be true, we would expect the arrays deemed type 1 at endpoint to eventually become fully encapsulated within the headcaps (as is the case for type 2 implants at week 12) if endpoint were to be extended. The comparable timing of performance decline in type 2 animals provides evidence for the latter, that type 2 implants became such upon implantation.

By week 6 it is evident from the microCT data of an array from an animal sacrificed at 4 weeks that gross array displacement has already begun (Figure 2: top). All Type 2 animals fail to record single-units on all channels from week 6 onwards (Figure 4c), while single-units are absent on all channels of only one Type 1 rat following week 6. The diverging trends follow a sharp decline in both MU and SU performance for all animals between weeks 4–5 after which Type 1 MU yield levels off, but Type 2 MU yield continues to decline. The timing of this rapid decline in performance is consistent with a previous study using the same arrays in rats that reported solely 2 out of 10 animals recording single-units week 5 onwards while 8 out of 10 were recording units at week 3. Further, the authors noted that 6 of these arrays were found to be at least partially encapsulated with fibrous tissue [14]. The overall declining performance trends we observe from the outset are consistent with the aforementioned study as well as in studies using the same recording paradigm in mice [12, 14, 32]. Non-human primate studies, however, contrast these trends in that they report an increase in yield over the first 6 weeks, but are still subject to a high incidence of fibrous encapsulation at later time points (> 3 months) [4, 13]. This points towards an influence of

Author Manuscript Author Manuscript Author Manuscript Author Manuscript

factors on recording performance that are unique to the rodent model. Such factors may include anatomical and surgical differences, for example the dura of rhesus macaques is much thicker than that of rats and is sewn back atop the array and thus may physically delay meningeal ingrowth and gross array movement. Furthermore, the size of the implant relative to the rat brain is much greater versus that of a Utah array relative to a rhesus macaque brain. Thus, in the rat, a relatively higher percentage of vasculature would be disrupted upon implant thereby influencing encapsulation outcome [8, 10, 40]. Substantial differences in insertion induced vascular damage and subsequent variation in BBB leakage could, at least in part, explain the dichotomy of encapsulation severity.

The persisting significant evoked MU activity until study endpoint in both Type 1 and Type 2 animals despite low to nil SU yield and array ejection highlights the value in MU analysis. The sustained MU yield following declining SU yield is also evident in a previous study using the same recording paradigm, but with linear probes in mice. Unsortable threshold crossings can contribute not only to a prolonged performance comparison, but may also carry meaningful signals for a bandwidth based decoding approach in lieu of SU sorting [41].

4.3 Unique impedance spectra features between encapsulation types

Significantly different impedance behavior is evident upon separation of animals into encapsulation types. Differences become apparent with significantly greater Type 1 magnitude impedance (Figure 5b) by the second week following implantation and persist throughout study duration. Such are apparent at much earlier time points than the divergence of electrophysiology performance that occurs at week 6 (Figure 4). A comparison of Nyquist traces over time between representative animals from each encapsulation type reveal a pronounced semicircular feature extending from mid-to-high frequencies present both at early and late time points in the Type 1 implant (Figure 6a) consistent with averaged traces at weeks 2 onward (7&8: left). In Type 2 arrays the semicircular feature is evident with a smaller diameter over a narrow range of high frequencies (Figure 6b).

Equivalent circuit modeling of the complex impedance spectra can help further understand the different elements of the neural electrode tissue interface[42–45]. In his dissertation, J.C. Williams independently varies each of the most relevant model parameters and plots the resulting change in Nyquist traces. When the extracellular resistance parameter (R_{ex}) of the cellular component of the circuit model is increased, it results in an increase in the diameter of the semicircular feature and a northeast shift in impedance at 1 kHz [45] (see Appendix C of the dissertation). This semicircular feature is more prominent in Type 1 arrays with a greater diameter and farther shifted 1 kHz impedance compared to Type 2 arrays, suggesting greater extracellular resistance in Type 1 arrays due to the cellular component between the electrode tips and ground screw. In the representative channel, this feature is most prominent at early time points, however upon inspection of single traces from other implants, it is greatest at varying time points between animals. Averaged traces over weeks between types show that the difference between types is evident at week 2 and persists until endpoint (Figure 7&8: left). This in conjunction with the resistive trend at low frequencies in Type 2 implants at week 0, point to unique tissue environments between encapsulation types that

Author Manuscript Author Manuscript Author Manuscript Author Manuscript

begin at acute time points, persist to chronic endpoint, and coincide with significant differences in electrophysiology performance that become apparent at 6 weeks (Figure 4).

In taking into consideration the less pronounced Nyquist feature (as attributable to R_{ex}) of Type 2 arrays with the significantly lower impedance magnitude recordings at 1 kHz, we begin to obtain a basis upon which to distinguish the tissue environment between types without the need for histological analysis at multiple end points. A lower extracellular resistive component would point towards a less resistive path to ground that could be attributable to reduced tissue cell density consistent with lower magnitude impedance at 1 kHz. The differences between Type 1 and Type 2 tissue environments may be related to what is observed in a study of the impedance properties of healthy versus infarct myocardium (heart tissue) respectively [46]. As collagen content of infarct myocardium increases, the impedance magnitude at frequencies at and below 1 kHz significantly decreases. Similarly, in Type 2 implants, impedance magnitude at 1 kHz is significantly lower (Figure 5) than in Type 1 implants and, as evident in the Bode plots (Figure 7) at later 8-week and 12-week time points and not at acute time points, the lower impedance magnitudes are evident over a wide bandwidth. Given that the reduced impedance magnitude is coincident with greater collagenous encapsulation at endpoint (Figure 1 and 5) in addition to the aforementioned impedance features that correspond to lower R_{ex}, fibrotic/meningeal ingrowth would be expected as early as week 2 and could contribute to gross array movement as observed at week 4 (Figure 2) [4, 13]. Upon observation of mesh micro-ECoG grids implanted in rats through a cranial window, Schendel et al report encapsulation tissue progression that aligns with these estimated time points. They observe the formation of initially avascular fibrous tissue at 7 days post-implant that thickens and forms vasculature by 28 days post-implant [19]. Thus, such impedance features along with electrophysiology performance differences (as observed between types) may be used as early markers for assessing array outcome.

4.4 Array encapsulation prevalence and intervention strategies

Meningeal encapsulation, the hallmark of the most prevalent chronic biological failure mode, occurred in greater proportion and on an accelerated time course in our model when compared to primate MEA models [4]. In all animals we observed array extrusion into the headcap and if not complete, substantial meningeal encapsulation such that only a portion of the array protruded by endpoint at 12-weeks. In a comprehensive primate MEA failure mode study, Barrese et. al. observed meningeal encapsulation with array extrusion in about half of the chronic array failures that occurred on average by 23 weeks post implant. As we observed in our model, these failed primate MEA arrays had been progressively worsening in recording performance leading up to failure. Despite substantial to full encapsulation, all arrays in our study recorded significant MU activity upon the last recording session. If we extrapolate our model to the primate model, this would suggest the MEAs could have been fully encapsulated and ejected before meeting the failure criterion.

Encapsulation and eventual extrusion is a result of a combination of factors: infiltrating fibroblasts from arachnoid and dura mater, and dura regrowth [13, 47]. Varying vascular damage upon implantation could influence the rate and degree of fibroblast influx to thereby yield distinct encapsulation types. Both physical [48] and pharmacological approaches [47,

Author Manuscript Author Manuscript Author Manuscript Author Manuscript

49] to combat meningeal extrusion of commercial Utah model arrays have been described, but without enough success to be used consistently in practice [4]. Our findings highlight the need for strategies to prevent array encapsulation and extrusion.

5. Conclusion

These data demonstrate that L1CAM yields significant recording benefits at acute time points in a model relatable to conventional non-human primate studies, but motivate additional chronic studies owing to a high prevalence of array encapsulation and array ejection resulting in poor recording yield. Encapsulation outcome is respective of recording performance throughout the study. These data also suggest that impedance spectra may be used in conjunction with electrophysiology metrics as markers to trace the implant tissue environment and predict encapsulation outcome.

Supplementary Material

Refer to Web version on PubMed Central for supplementary material.

Acknowledgments

The authors appreciate the guidance of Dr. Yijen Wu, director of the Animal Imaging Core at Rangos Research Center at Children's Hospital of Pittsburgh of UPMC, in acquiring and analyzing microCT images. This work was supported by NIH NINDS R01NS094396, R01NS062019, and R01NS089688.

References

1. Normann RA, Fernandez E. Clinical applications of penetrating neural interfaces and Utah Electrode Array technologies. J Neural Eng. 2016; 13(6):061003. [PubMed: 27762237]
2. Gunasekera, Bhagya, Saxena, Tarun, Bellamkonda, Ravi, Karumbaiah, Lohitash. Intracortical Recording Interfaces: Current Challenges to Chronic Recording Function. ACS Chemical Neuroscience. 2015; 6(1):68–83. [PubMed: 25587704]
3. Hatsopoulos NG, Donoghue JP. The science of neural interface systems. Annu Rev Neurosci. 2009; 32:249–66. [PubMed: 19400719]
4. Barrese JC, Rao N, Paroo K, Triebwasser C, Vargas-Irwin C, Franquemont L, Donoghue JP. Failure mode analysis of silicon-based intracortical microelectrode arrays in non-human primates. J Neural Eng. 2013; 10(6):066014. [PubMed: 24216311]
5. Chestek Cynthia A, Vikash Gilja, Paul Nuyujukian, Foster Justin D, Fan Joline M, Kaufman Matthew T, Churchland Mark M, Zuley Rivera-Alvidrez, Cunningham John P, Ryu Stephen I, Shenoy Krishna V. Long-term stability of neural prosthetic control signals from silicon cortical arrays in rhesus macaque motor cortex. Journal of Neural Engineering. 2011; 8(4):045005. [PubMed: 21775782]
6. Wellman, Steven M., Eles, James R., Ludwig, Kip A., Seymour, John P., Michelson, Nicholas J., Mcfadden, William E., Vazquez, Alberto L., Kozai, Takashi Dy. Advanced Functional Materials. 2017. A Materials Roadmap to Functional Neural Interface Design.
7. Kozai TD, Jaquins-Gerstl AS, Vazquez AL, Michael AC, Cui XT. Brain tissue responses to neural implants impact signal sensitivity and intervention strategies. ACS Chem Neurosci. 2015; 6(1):48–67. [PubMed: 25546652]
8. Kozai TD, Marzullo TC, Hooi F, Langhals NB, Majewska AK, Brown EB, Kipke DR. Reduction of neurovascular damage resulting from microelectrode insertion into the cerebral cortex using in vivo two-photon mapping. J Neural Eng. 2010; 7(4):046011. [PubMed: 20644246]
9. Ravikumar M, Sunil S, Black J, Barkauskas DS, Haung AY, Miller RH, Selkirk SM, Capadona JR. The roles of blood-derived macrophages and resident microglia in the neuroinflammatory response

Author Manuscript Author Manuscript Author Manuscript Author Manuscript

to implanted intracortical microelectrodes. Biomaterials. 2014; 35(28):8049–64. [PubMed: 24973296]

10. Kozai TD, Vazquez AL, Weaver CL, Kim SG, Cui XT. In vivo two-photon microscopy reveals immediate microglial reaction to implantation of microelectrode through extension of processes. J Neural Eng. 2012; 9(6):066001. [PubMed: 23075490]
11. Schwartz, Andrew B., Tracy Cui, X., Weber, Douglas j, Moran, Daniel W. Brain-Controlled Interfaces: Movement Restoration with Neural Prosthetics. Neuron. 2006; 52(1):205–220. [PubMed: 17015237]
12. Kozai TD, Li X, Bodily LM, Caparosa EM, Zenonos GA, Carlisle DL, Friedlander RM, Cui XT. Effects of caspase-1 knockout on chronic neural recording quality and longevity: Insight into cellular and molecular mechanisms of the reactive tissue response. Biomaterials. 2014; 35(36): 9620–34. [PubMed: 25176060]
13. Degenhart AD, Eles J, Dum R, Mischel JL, Smalianchuk I, Endler B, Ashmore RC, Tyler-Kabara EC, Hatsopoulos NG, Wang W, Batista AP, Cui XT. Histological evaluation of a chronically-implanted electrocorticographic electrode grid in a non-human primate. J Neural Eng. 2016; 13(4): 046019. [PubMed: 27351722]
14. Nolta NF, Christensen MB, Crane PD, Skousen JL, Tresco PA. BBB leakage, astrogliosis, and tissue loss correlate with silicon microelectrode array recording performance. Biomaterials. 2015; 53:753–62. [PubMed: 25890770]
15. Woolley AJ, Desai HA, Otto KJ. Chronic intracortical microelectrode arrays induce non-uniform, depth-related tissue responses. J Neural Eng. 2013; 10(2):026007. [PubMed: 23428842]
16. Rousche, Patrick J., Normann, Richard A. Chronic recording capability of the Utah Intracortical Electrode Array in cat sensory cortex. Journal of Neuroscience Methods. 1998; 82(1):1–15. [PubMed: 10223510]
17. Kozai, Takashi DY., Eles, James R., Vazquez, Alberto L., Tracy Cui, X. Two-photon imaging of chronically implanted neural electrodes: Sealing methods and new insights. Journal of Neuroscience Methods. 2016; 256:46–55.
18. Kozai TD, Langhals NB, Patel PR, Deng X, Zhang H, Smith KL, Lahann J, Kotov NA, Kipke DR. Ultrasmall implantable composite microelectrodes with bioactive surfaces for chronic neural interfaces. Nat Mater. 2012; 11(12):1065–73. [PubMed: 23142839]
19. Schendel, Amelia A., Nonte, Michael W., Vokoun, Corinne, Richner, Thomas J., Brodnick, Sarah K., Atry, Farid, Frye, Seth, Bostrom, Paige, Pashaie, Ramin, Thongpang, Sanitta, Eliceiri, Kevin W., Williams, Justin C. The effect of micro-ECoG substrate footprint on the meningeal tissue response. Journal of neural engineering. 2014; 11(4):046011–046011. [PubMed: 24941335]
20. Patel PR, Zhang H, Robbins MT, Nofar JB, Marshall SP, Kobylarek MJ, Kozai TD, Kotov NA, Chestek CA. Chronic in vivo stability assessment of carbon fiber microelectrode arrays. J Neural Eng. 2016; 13(6):066002. [PubMed: 27705958]
21. Woolley AJ, Desai HA, Steckbeck MA, Patel NK, Otto KJ. In situ characterization of the brain-microdevice interface using device-capture histology. J Neurosci Methods. 2011; 201(1):67–77. [PubMed: 21802446]
22. Alba, Nicolas, Du, Zhanhong, Catt, Kasey, Kozai, Takashi, Cui, X. In Vivo Electrochemical Analysis of a PEDOT/MWCNT Neural Electrode Coating. Biosensors. 2015; 5(4):618. [PubMed: 26473938]
23. Luo X, Matranga C, Tan S, Alba N, Cui XT. Carbon nanotube nanoreservior for controlled release of anti-inflammatory dexamethasone. Biomaterials. 2011; 32(26):6316–23. [PubMed: 21636128]
24. Zhang Z, Yoo R, Wells M, Beebe TP Jr, Biran R, Tresco P. Neurite outgrowth on well-characterized surfaces: preparation and characterization of chemically and spatially controlled fibronectin and RGD substrates with good bioactivity. Biomaterials. 2005; 26(1):47–61. [PubMed: 15193880]
25. Azemi E, Lagenaur CF, Cui XT. The surface immobilization of the neural adhesion molecule L1 on neural probes and its effect on neuronal density and gliosis at the probe/tissue interface. Biomaterials. 2011; 32(3):681–92. [PubMed: 20933270]

Author Manuscript Author Manuscript Author Manuscript Author Manuscript

26. Azemi E, Stauffer WR, Gostock MS, Lagenaur CF, Cui XT. Surface immobilization of neural adhesion molecule L1 for improving the biocompatibility of chronic neural probes: In vitro characterization. Acta Biomater. 2008; 4(5):1208–17. [PubMed: 18420473]
27. He W, Mcconnell GC, Bellamkonda RV. Nanoscale laminin coating modulates cortical scarring response around implanted silicon microelectrode arrays. J Neural Eng. 2006; 3(4):316–26. [PubMed: 17124336]
28. Azemi E, Gobbel GT, Cui XT. Seeding neural progenitor cells on silicon-based neural probes. J Neurosurg. 2010; 113(3):673–81. [PubMed: 20151783]
29. Tate, Ciara C., Shear, Deborah A., Tate, Matthew C., Archer, David R., Stein, Donald G., Laplaca, Michelle C. Laminin and fibronectin scaffolds enhance neural stem cell transplantation into the injured brain. Journal of Tissue Engineering and Regenerative Medicine. 2009; 3(3):208–217. [PubMed: 19229887]
30. Lagenaur C, Lemmon V. An L1-like molecule, the 8D9 antigen, is a potent substrate for neurite extension. Proc Natl Acad Sci U S A. 1987; 84(21):7753–7. [PubMed: 3478724]
31. Kolarcik CL, Bourbeau D, Azemi E, Rost E, Zhang L, Lagenaur CF, Weber DJ, Cui XT. In vivo effects of L1 coating on inflammation and neuronal health at the electrode-tissue interface in rat spinal cord and dorsal root ganglion. Acta Biomater. 2012; 8(10):3561–75. [PubMed: 22750248]
32. Kozai, Takashi DY., Du, Zhanhong, Gugel, Zhannetta V., Smith, Matthew A., Chase, Steven M., Bodily, Lance M., Caparosa, Ellen M., Friedlander, Robert M., Tracy Cui, X. Comprehensive chronic laminar single-unit, multi-unit, and local field potential recording performance with planar single shank electrode arrays. Journal of Neuroscience Methods. 2015; 242:15–40. [PubMed: 25542351]
33. Lee CD, Hara SA, Yu L, Kuo JT, Kim BJ, Hoang T, Pikov V, Meng E. Matrigel coatings for Parylene sheath neural probes. J Biomed Mater Res B Appl Biomater. 2016; 104(2):357–68. [PubMed: 25809504]
34. Kozai TD, Eles JR, Vazquez AL, Cui XT. Two-photon imaging of chronically implanted neural electrodes: Sealing methods and new insights. J Neurosci Methods. 2016; 258:46–55. [PubMed: 26526459]
35. Eles JR, Vazquez AL, Snyder NR, Lagenaur C, Murphy MC, Kozai TD, Cui XT. Neuroadhesive L1 coating attenuates acute microglial attachment to neural electrodes as revealed by live two-photon microscopy. Biomaterials. 2017; 113:279–292. [PubMed: 27837661]
36. Bechade, Catherine, Cantaut-Belarif, Yasmine, Bessis, Alain. Microglial control of neuronal activity. Frontiers in Cellular Neuroscience. 2013; 7:32. [PubMed: 23543873]
37. Golda M, Brzychczy-Wloch M, Faryna M, Engvall K, Kotarba A. Oxygen plasma functionalization of parylene C coating for implants surface: nanotopography and active sites for drug anchoring. Mater Sci Eng C Mater Biol Appl. 2013; 33(7):4221–7. [PubMed: 23910336]
38. Bilek, Marcela M., Mckenzie, David R. Plasma modified surfaces for covalent immobilization of functional biomolecules in the absence of chemical linkers: towards better biosensors and a new generation of medical implants. Biophysical Reviews. 2010; 2(2):55–65. [PubMed: 28510008]
39. Bhatia SK, Shriver-Lake LC, Prior KJ, Georger JH, Calvert JM, Bredehorst R, Ligler FS. Use of thiol-terminal silanes and heterobifunctional crosslinkers for immobilization of antibodies on silica surfaces. Anal Biochem. 1989; 178(2):408–13. [PubMed: 2546467]
40. Karumbaiah L, Saxena T, Carlson D, Patil K, Patkar R, Gaupp EA, Betancur M, Stanley GB, Carin L, Bellamkonda RV. Relationship between intracortical electrode design and chronic recording function. Biomaterials. 2013; 34(33):8061–74. [PubMed: 23891081]
41. Irwin ZT, Thompson DE, Schroeder KE, Tat DM, Hassani A, Bullard AJ, Woo SL, Urbanchek MG, Sachs AJ, Cederna PS, Stacey WC, Patil PG, Chestek CA. Enabling Low-Power, Multi-Modal Neural Interfaces Through a Common, Low-Bandwidth Feature Space. IEEE Trans Neural Syst Rehabil Eng. 2016; 24(5):521–31. [PubMed: 26600160]
42. Williams JC, Hippensteel JA, Dilgen J, Shain W, Kipke DR. Complex impedance spectroscopy for monitoring tissue responses to inserted neural implants. J Neural Eng. 2007; 4(4):410–23. [PubMed: 18057508]

Author Manuscript Author Manuscript Author Manuscript Author Manuscript

43. Otto KJ, Johnson MD, Kipke DR. Voltage pulses change neural interface properties and improve unit recordings with chronically implanted microelectrodes. IEEE Trans Biomed Eng. 2006; 53(2): 333–40. [PubMed: 16485763]
44. Malaga, Karlo A., Schroeder, Karen E., Patel, Paras R., Irwin, Zachary T., Thompson, David E., Nicole Bentley, J., Lempka, Scott F., Chestek, Cynthia A., Patil, Parag G. Data-driven model comparing the effects of glial scarring and interface interactions on chronic neural recordings in non-human primates. Journal of Neural Engineering. 2016; 13(1):016010. [PubMed: 26655972]
45. Williams, JC. Performance of Chronic Neural Implants: Measurement, Modeling and Intervention Strategies. Arizona State University; 2001.
46. Schwartzman D, Chang I, Michele JJ, Mirotznik MS, Foster KR. Electrical impedance properties of normal and chronically infarcted left ventricular myocardium. J Interv Card Electrophysiol. 1999; 3(3):213–24. [PubMed: 10490477]
47. Shearer, Morven C., Fawcett, James W. The astrocyte/meningeal cell interface – a barrier to successful nerve regeneration? Cell and Tissue Research. 2001; 305(2):267–273. [PubMed: 11545264]
48. Maynard EM, Fernandez E, Normann RA. A technique to prevent dural adhesions to chronically implanted microelectrode arrays. J Neurosci Methods. 2000; 97(2):93–101. [PubMed: 10788663]
49. Li, Ping, Allen, Hamish, Banerjee, Subhashis, Franklin, Simon, Herzog, Linda, Johnston, Cynthia, Mcdowell, Jack, Paskind, Michael, Rodman, Laura, Salfeld, Jochen, Towne, Elizabeth, Tracey, Daniel, Wardwell, Scott, Wei, Feng-Yi, Wong, Winnie, Kamen, Robert, Seshadri, Tara. Mice deficient in IL-1β-converting enzyme are defective in production of mature IL-1β and resistant to endotoxic shock. Cell. 1995; 80(3):401–411. [PubMed: 7859282]

Author Manuscript Author Manuscript Author Manuscript Author Manuscript

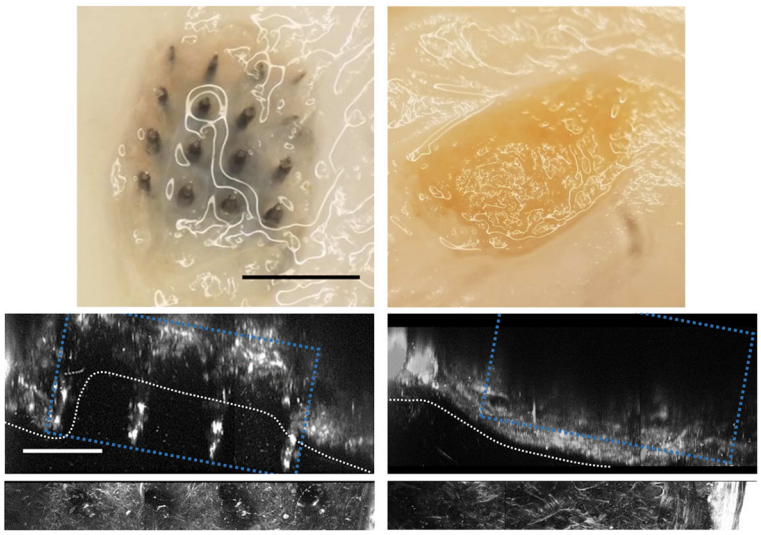

Figure 1.

Ejection types from representative uncoated arrays. Left: Type 1, Right: Type 2. Top: Image of ventral surface (underside) of headcap. Black scale bar = 1 mm. Bottom: SHG imaging at sagittal view of tissue surrounding immediate implant area within headcap. White bracket indicates protrusion from white dotted line that spans the craniotomy. White scale bar = 400 μm. Blue dotted box indicates probe location and white dotted highlights meningeal surface.

Author Manuscript Author Manuscript Author Manuscript Author Manuscript

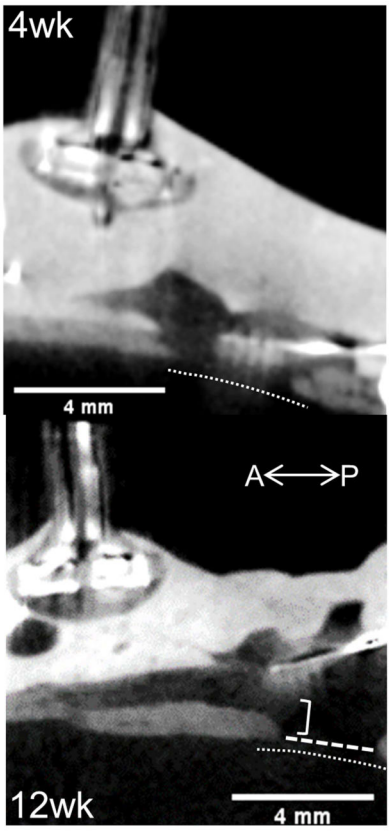

Figure 2.

Sagittal microCT imaging of uncoated implants following perfusion, but preceding dissection (intact head). Top: 4 weeks post-implantation Bottom: 12 weeks. Implant bed and shanks visible from right side of image near craniotomy opening in skull (bottom right area of each image). Thin dotted line indicates brain tissue surface, wide dotted line spans craniotomy, bracket highlights implant displacement.

Author Manuscript Author Manuscript Author Manuscript Author Manuscript

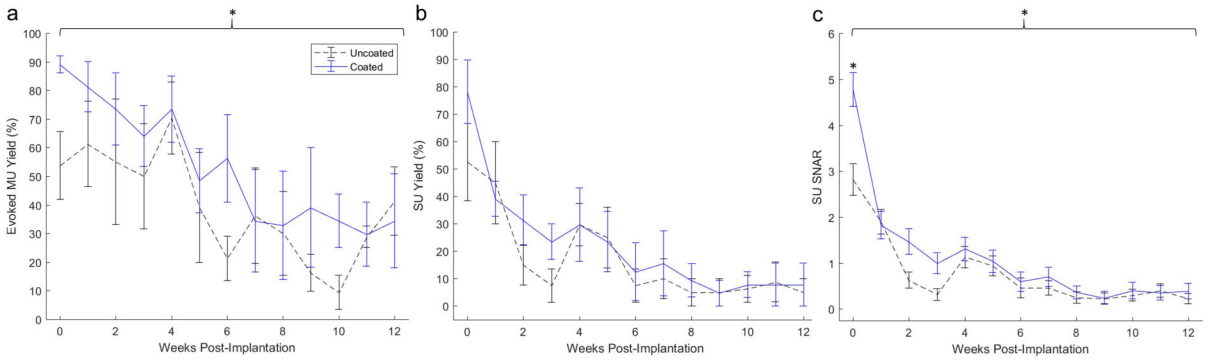

Figure 3.

Electrophysiological performance of L1CAM coated arrays (blue) compared to uncoated control arrays (black dashed). Average evoked multi-unit yield (a), single-unit yield (b), and single-unit signal-to-noise amplitude ratio (c) between treatment groups from weekly recordings over a 12-week period. Brackets indicate significant overall (group-wise) treatment effects with $p = 0.0114$ and $p < 0.0001$ for a and c respectively. * indicates significant difference with $p<0.001$ from Bonferroni corrected pair-wise test.

Author Manuscript Author Manuscript Author Manuscript Author Manuscript

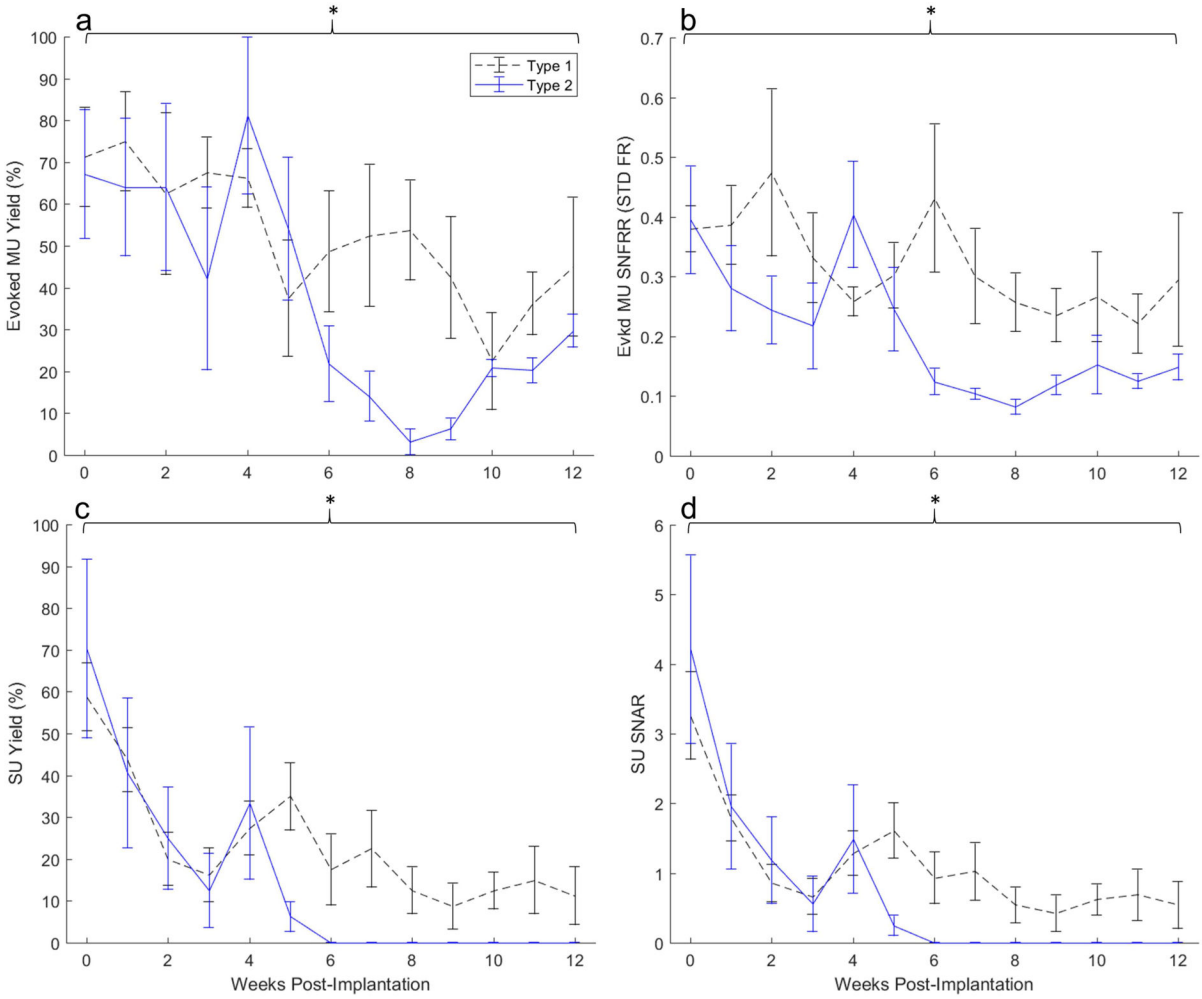

Figure 4.

Electrophysiological performance of Type 1 encapsulated arrays (black dashed) compared Type 2 (blue). Average evoked multi-unit yield (a), evoked multi-unit signal-to-noise firing rate ratio (b), single-unit yield (c), and single-unit signal-to-noise amplitude ratio (d) between encapsulation groups from weekly recordings over a 12-week period. Brackets indicate an overall (group-wise) significant treatment effect of encapsulation type on MU yield, MU SNFRR, SU yield, and SU SNAR ($p = 0.0038$, $p = 0.0001$, $p = 0.0099$, and $p = 0.0472$ respectively.

Author Manuscript Author Manuscript Author Manuscript Author Manuscript

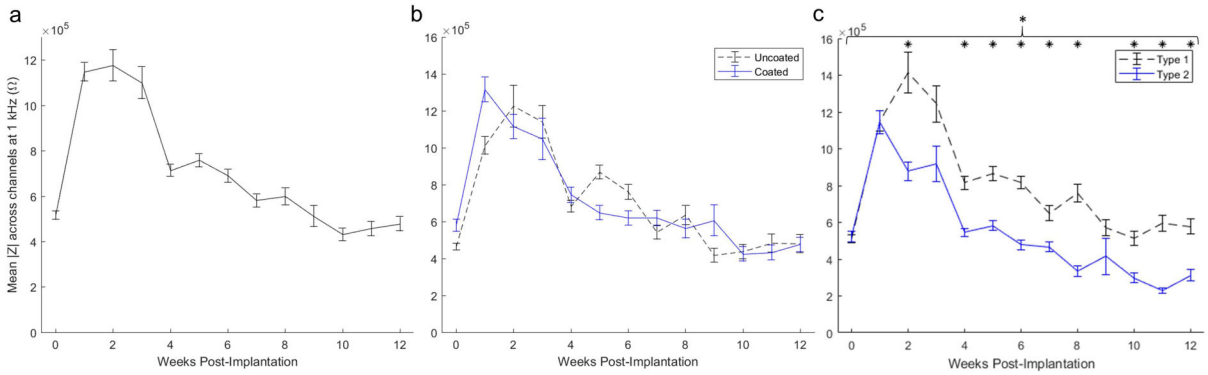

Figure 5.

Mean magnitude impedance across all channels from all animals (a), mean magnitude impedance across channels between coating treatments (b) and encapsulation types (c). * indicates significant difference on weeks 0, 4–8, and 10–12 with $p < 0.002$ from Bonferroni corrected pair-wise test. Note lower impedance from Type 2 implants following week 1.

Author Manuscript Author Manuscript Author Manuscript Author Manuscript

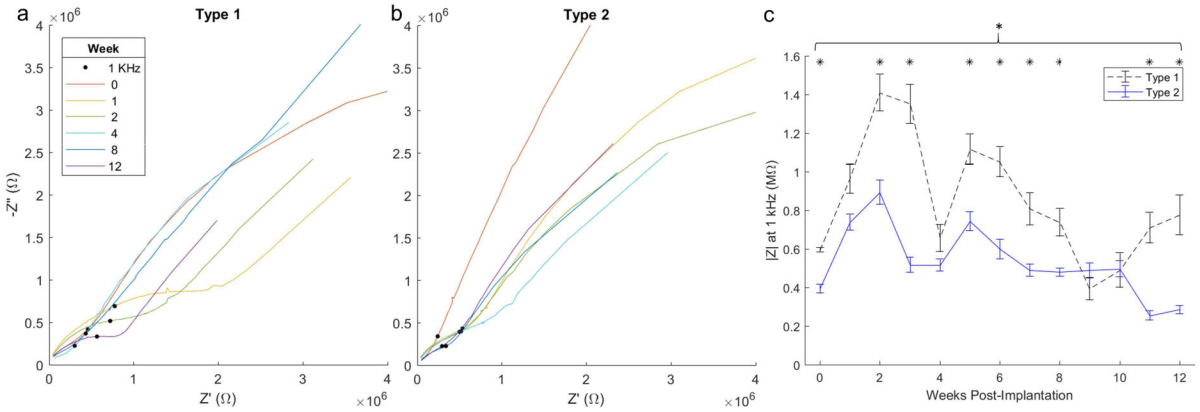

Figure 6.

Nyquist plots (a–b) of the same channel over time from representative Type 1 (left) and Type 2 (right) arrays. Black dot indicates impedance at 1 kHz. Magnitude impedance (c) at 1 kHz from the same implants averaged across channels over time. Bracket indicates group-wise encapsulation effect ($p < 0.001$), and * indicates significant difference on weeks 0, 3–4, 5–8, and 11–12 with $p < 0.002$ from Bonferroni corrected pair-wise test. Note a more pronounced semicircular feature at the high impedance region of Type 1 arrays accompanied by a northeast shift in impedance at 1 kHz.

Author Manuscript Author Manuscript Author Manuscript Author Manuscript

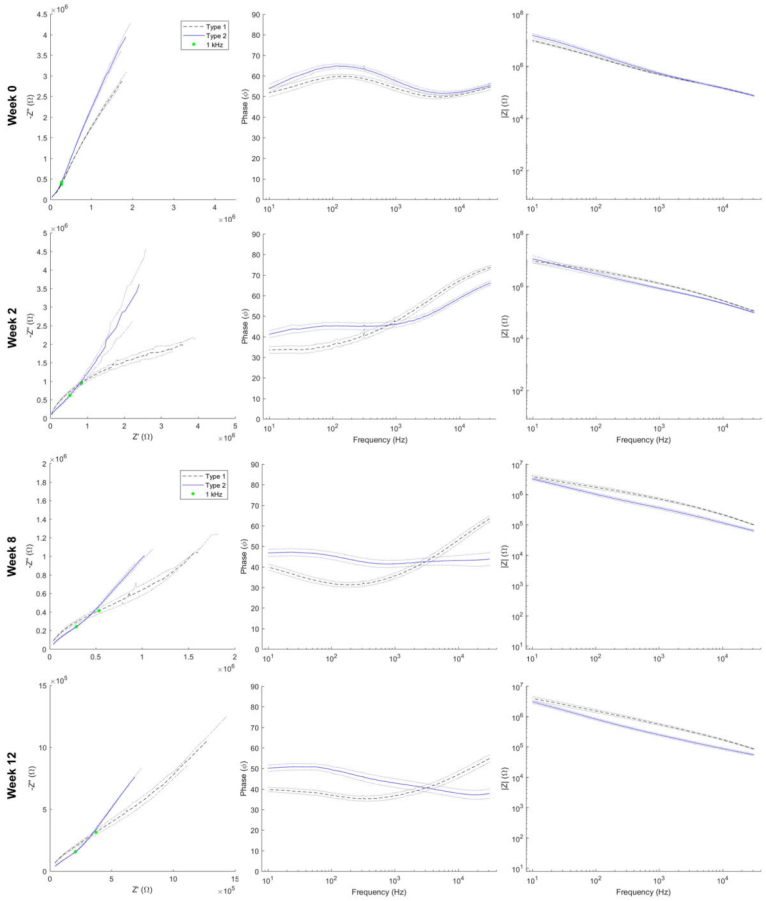

Figure 7.

Nyquist (left), phase (middle), and Bode (right) traces averaged across all channels between types at week 0, 2, 8 and 12. Dotted lines indicate ± SEM. Green dot indicates impedance at 1 kHz. Note more pronounced high impedance semicircular feature in Type 1 averaged Nyquist traces week 2 onward, trend for lower phase below 1 kHz for Type 2 implants, and lower magnitude impedance from Type 2 arrays across a broad range of frequencies from week 2 onward.

Author Manuscript

Author Manuscript

Author Manuscript

Author Manuscript

Table 1

Number of implants by treatment type.

	L1CAM	Uncoated
Type I	2	3
Type II	2	2